

Forward production of prompt neutrinos from charm in the atmosphere and at high energy colliders

Weidong Bai,^a Milind Diwan,^b Maria Vittoria Garzelli,^c Yu Seon Jeong,^d
Karan Kumar,^{b,e,1} Mary Hall Reno^f

^a*School of Physics, Sun Yat-sen University, Guangzhou, Guangdong 510275, P. R. China*

^b*Brookhaven National Laboratory, Upton, New York, USA*

^c*II Institut für Theoretische Physik, Universität Hamburg
Luruper Chaussee 149, D-22761, Hamburg, Germany*

^d*High Energy Physics Center, Chung-Ang University, Dongjak-gu, Seoul 06974, Republic of Korea*

^e*Department of Physics and Astronomy, Stony Brook University, Stony Brook, NY 11794, USA*

^f*Department of Physics and Astronomy, University of Iowa, Iowa City, IA 52242, USA*

E-mail: baiwd3@mail.sysu.edu.cn, diwan@bnl.gov,
maria.vittoria.garzelli@desy.de, yusjeong@cau.ac.kr, fk237@cornell.edu,
mary-hall-reno@uiowa.edu

ABSTRACT: The high-energy atmospheric neutrino flux is dominated by neutrinos from the decays of charmed hadrons produced in the forward direction by cosmic ray interactions with air nuclei. We evaluate the charm contributions to the prompt atmospheric neutrino flux as a function of the center-of-mass energy \sqrt{s} of the hadronic collision and of the center-of-mass rapidity y of the produced charm hadron. Uncertainties associated with parton distribution functions are also evaluated as a function of y . We find that the y coverage of LHCb for forward heavy-flavour production, complemented by the angular coverage of present and future forward neutrino experiments at the LHC, bracket the most interesting y regions for the prompt atmospheric neutrino flux. At $\sqrt{s} = 14$ TeV foreseen for the HL-LHC phase, nucleon collisions in air contribute to the prompt neutrino flux prominently below $E_\nu \sim 10^7$ GeV. Measurements of forward charm and/or forward neutrinos produced in hadron collisions up to $\sqrt{s} = 100$ TeV, which might become possible at the FCC, are relevant for the prompt atmospheric neutrino flux up to $E_\nu = 10^8$ GeV and beyond.

¹Department of Physics, Cornell University, Ithaca, NY 14853, USA

Contents

1	Introduction	1
2	Prompt atmospheric neutrino fluxes	4
2.1	Cascade equations	4
2.2	Cosmic ray spectrum	6
3	Z-moments and atmospheric neutrino fluxes from charm	6
3.1	Z-moments for charm hadron production	6
3.2	Z-moments and FPF neutrinos	11
3.3	Atmospheric neutrino fluxes from charm hadrons	14
4	Uncertainty from the parton distribution functions	16
5	Discussion and conclusions	19

1 Introduction

Through the detection of neutrinos produced in the Sun, in the atmosphere, in reactors and in laboratory beams, information concerning neutrino properties has been inferred with increasing precision over the years [1]. Ongoing and future experiments that use these neutrinos will refine some of the already existing measurements, provide new ones, expand our knowledge of the Standard Model (SM) of interactions and probe parameter spaces of new physics beyond the Standard Model (BSM) [2]. Data on neutrino interactions are useful to constrain the partonic structure of nucleons and nuclei. Direct neutrino cross-section measurements using laboratory neutrino beams have been made, so far, for neutrino energies up to $E_\nu = 360$ GeV [3]. Neutrino cross-section measurements extracted from energy and angular distributions of neutrino events in the IceCube detector have extended cross-section measurements to $E_\nu \sim 1$ PeV, however, with large uncertainties [4, 5]. On the other hand, programs for studying neutrino oscillation physics with laboratory neutrino beams focus on neutrino beam average energies up to 17 GeV [3]. Oscillation physics is also part of the research program of neutrino telescopes [6–8] and other underground detectors [9, 10].

The highest energy neutrinos in the laboratory are produced at hadron colliders. As already discussed in the 1980’s and 1990’s, there is a large flux of neutrinos that goes in the very forward direction [11–14]. The highest energy electron and tau (anti)neutrinos in the forward region come from the production and decays of heavy-flavour hadrons, especially charm hadrons [15–18]. Over the past few years, two experiments at the Large Hadron

Collider (LHC), FASER ν [19, 20] and SND@LHC [21, 22], have been prepared to detect such neutrinos with energies up to a few TeV and investigate related physics. These experiments are installed in existing service tunnels and have started collecting data during Run 3 at the LHC. A prototype detector for FASER ν recorded the first few candidate neutrino events during the LHC Run 2 [23]. A next-generation of forward neutrino experiments for the High-Luminosity runs of the LHC (HL-LHC) has also recently been proposed. Most of them could be located into a purpose-built Forward Physics Facility (FPF) [24, 25], but further solutions, involving other LHC areas and neutrino pseudo-rapidities, $\eta_\nu = -\ln \tan(\theta/2)$ where θ is the angle relative to the beam direction, are also under investigation. Neutrino experiments at the FPF would consist of upgrades of the Run 3 experiments with the FASER ν 2 and the FAR Advanced SND (AdvSND) detectors, plus a liquid Argon time projection chamber called FLArE. The FPF location is planned for a site at a distance of $\sim 620 - 685$ m from the ATLAS interaction point, and will have sizes that allow to cover forward neutrino pseudo-rapidities down to approximately $\eta_\nu \gtrsim 7$ [25]. A second AdvSND detector, called NEAR, installed outside the FPF and closer to one of the LHC IP, is planned to cover neutrino rapidities in the range $4 < \eta_\nu < 5$ [25]. Over a baseline of $620 - 685$ m, oscillations among active neutrinos are minimal, but oscillations between active and sterile neutrinos with masses of the order of 10's of eV can be investigated [15].

Neutrinos are also interesting from the point of view of astrophysics [26]. Measurements of the diffuse flux of astrophysical neutrinos have opened a window on high-energy neutrino sources [27–29]. An important background to the diffuse flux is the flux of neutrinos produced in cosmic ray interactions in the atmosphere. The so-called “conventional” atmospheric flux comes from the decays of charged pions (π^\pm) and kaons (K^\pm) produced in these interactions. As their decay lengths increase with energy, pions and kaons are apt to lose energy through interactions with other particles before they decay [30, 31]. The resulting conventional neutrino flux steeply falls as energy increases.

A portion of atmospheric neutrinos also comes from prompt heavy-flavour hadron decays, predominantly from charm mesons. The flux of prompt atmospheric neutrinos has a harder spectrum than the conventional one due to very short lifetime of heavy-flavour hadrons. Accordingly, the prompt neutrino flux becomes more important than the conventional neutrino flux at a sufficiently high energy. One feature of both the prompt and conventional components of the atmospheric neutrino flux is that the energies of hadrons most important to the atmospheric neutrino flux carry large fractions of the energies of the cosmic rays primaries impinging on the atmosphere and interacting with the atmospheric nuclei. This is a consequence of the fact that the spectrum of high-energy cosmic rays falls steeply according to a power law $\sim E^{-2.7} - E^{-3}$. Various theoretical evaluations [32–39] indicate that the flux of prompt atmospheric neutrinos dominates over the conventional one above $E_\nu \sim 10^5 - 10^6$ GeV. To date, the atmospheric neutrino spectra inferred by experimental observations seem to be consistent with the conventional component, the flux of which is dominant at relatively low energies. Although upper limits have been established [29, 40], a definitive measurement of the prompt atmospheric neutrino flux has not yet been made.

On the other hand, theoretical predictions of the prompt atmospheric neutrino fluxes have large uncertainties, mainly due to a poor understanding of heavy flavour production [32–39]. As we will discuss in the following of this work, the production of high-energy neutrinos in the atmosphere has some kinematic overlap with the production of neutrinos in the forward region at the LHC. The $\sqrt{s} = 14$ TeV collision energy foreseen for the HL-LHC phase, corresponds to a cosmic ray nucleon energy $E_p \sim 10^8$ GeV on a fixed-target (air) nucleon. Through production and decays of hadrons, these high-energy cosmic ray interactions in the atmosphere yield neutrinos in the energy range where the prompt component is the most important part of the atmospheric neutrino flux. On the other hand, with the high luminosity upgrade that will be a factor of 20 times the luminosity of Run 3, the LHC can produce an abundant number of prompt neutrino events in the forward region, through the interaction of forward prompt neutrinos with the nuclear targets of forthcoming experiments [25]. Therefore, measurements of heavy flavour and/or prompt neutrino production at forward LHC experiments can contribute to reduce the uncertainty in the theoretical predictions of the prompt atmospheric neutrino fluxes.

The final aim of our work is to explore the connections of measurements of neutrinos and heavy hadrons at colliders with predictions of prompt neutrino fluxes in the atmosphere, and as a consequence, the potential utility of these measurements, with particular emphasis if neutrino measurements at the FPF, for neutrino astronomy applications. Towards this purpose, we examine in detail the overlap of kinematic regimes, extending our results of ref. [41], using as a basis a QCD evaluation of charm meson production cross sections, considering charm quark production at next-to-leading order (NLO) in perturbative QCD (pQCD) [42, 43] using the PROSA parton distribution functions (PDFs) [35] with parameters that make the results well-matched to the measurements by the LHCb experiment [44–46], accompanied by phenomenological fragmentation functions to describe the parton-to-meson transition and by analytical formulas for the evaluation of neutrino production in charmed meson decay [15, 47]. We examine the role played by collisions at different center-of-mass energies \sqrt{s} , up to a value of $\sqrt{s} = 100$ GeV foreseen for hadron-hadron interactions at a Future Circular Collider (FCC)[48, 49]. Since the neutrino pseudo-rapidity η_ν is correlated with the charm hadron rapidity y [16], we also consider the rapidity y of charm hadrons relevant to prompt atmospheric neutrino flux predictions. In the following, y will be used to refer to the charm hadron rapidity in the proton-proton center-of-mass (CM), or, equivalently, collider frame. We will also illustrate the impact of the small- x and large- x PDFs on the prompt neutrino fluxes.

The work is organized as follows. In section 2, the semi-analytic approach with Z -moments to determine the atmospheric neutrino fluxes from a set of coupled differential equations called cascade equations is reviewed. The cosmic ray spectra used as input in this work are also discussed in this section. In section 3, results for the Z -moment for charm hadron production and the atmospheric neutrino fluxes for different regions of \sqrt{s} and different intervals of collider-frame rapidity y of the parent charm hadrons are shown. Parton distribution function (PDF) uncertainties are illustrated and discussed in section 4. Finally,

conclusions are drawn in section 5.

2 Prompt atmospheric neutrino fluxes

2.1 Cascade equations

The atmospheric neutrino fluxes can be evaluated using the cascade equations and the so-called Z -moment method [30]. The cascade equations account for the propagation of the particles in the atmosphere, and the general expression is given by

$$\begin{aligned} \frac{d\phi_j(E, X)}{dX} &= -\frac{\phi_j(E, X)}{\lambda_j^{\text{int}}(E)} - \frac{\phi_j(E, X)}{\lambda_j^{\text{dec}}(E)} + \sum_k S(k \rightarrow j), \\ S(k \rightarrow j) &= \int_E^\infty dE' \frac{\phi_k(E', X)}{\lambda_k(E')} \frac{dn(k \rightarrow j; E', E)}{dE}. \end{aligned} \quad (2.1)$$

Here, $\phi_j(E, X)$ is the flux of particle j at the column depth X , and $\lambda_{j/k}^{\text{int}}$ and $\lambda_{j/k}^{\text{dec}}$ are the interaction and decay length for particle j (or k), respectively. In the source term $S(k \rightarrow j)$, $dn(k \rightarrow j; E', E)/dE$ depends on whether $k \rightarrow j$ proceeds through interactions or through decays with

$$\frac{dn(k \rightarrow j; E', E)}{dE} = \begin{cases} \frac{1}{\sigma_{kA}(E')} \frac{d\sigma(kA \rightarrow jY; E', E)}{dE} & (\text{interaction}) \\ \frac{1}{\Gamma_k(E')} \frac{d\Gamma(k \rightarrow jY; E', E)}{dE} & (\text{decay}), \end{cases} \quad (2.2)$$

so λ_k can be an interaction or decay length in the expression for $S(k \rightarrow j)$.

It is convenient to introduce the quantity $Z_{kj}(E)$. This so-called Z -moment is related to the spectrum-weighted differential cross section for particle production through interaction or decay and is defined as

$$Z_{kj}(E) \equiv \int_E^\infty dE' \frac{\phi_k(E', 0)}{\phi_k(E, 0)} \frac{\lambda_k(E)}{\lambda_k(E')} \frac{dn(k \rightarrow j; E', E)}{dE}. \quad (2.3)$$

Then, the source term $S(k \rightarrow j)$ in eq. (2.1) can be approximated in terms of the only energy-dependent Z -moment, the flux and the interaction (or decay) length of particle k , according to

$$S(k \rightarrow j) \simeq Z_{kj}(E) \frac{\phi_k(E, X)}{\lambda_k(E)} \quad (2.4)$$

under the assumption that $\phi_k(E', X)/\phi_k(E, X) \simeq \phi_k(E', 0)/\phi_k(E, 0)$. For cosmic ray nucleons, labeled here with $k = p$, this means that $\phi_p(E, X) \simeq \phi_p^0(E) f(X)$ where $\phi_p^0(E) = \phi_p(E, 0)$ is the cosmic ray flux at the top of the atmosphere and $f(X)$ describes its attenuation through the atmosphere which is largely energy independent and only depends on column depth X . The column depth depends on distance from the ground ℓ and zenith angle θ and is given by $X(\ell, \theta) = \int_\ell^\infty d\ell' \rho(h(\ell', \theta))$, where $h(\ell', \theta)$ is the altitude for a given (ℓ, θ) . The

atmospheric density is approximated by $\rho(h) = \rho_0 \exp(-h/h_0)$, where $h_0 = 6.4$ km and $\rho_0 h_0 = 1300$ g/cm².

The coupled cascade equations then consist of equations for incident cosmic rays, produced hadrons and neutrinos from the decays of hadrons. The atmospheric neutrino fluxes can be obtained by solving this system of coupled cascade equations. Two approximate solutions in terms of the Z -moments and incident cosmic ray spectrum in the low- and high-energy limits can be obtained at the surface of the Earth, with

$$\phi_{h \rightarrow \nu}^{\text{low}} = \sum_h \frac{Z_{ph} Z_{h\nu}}{1 - Z_{pp}} \phi_p^0, \quad (2.5)$$

$$\phi_{h \rightarrow \nu}^{\text{high}} = \sum_h \frac{Z_{ph} Z_{h\nu}}{1 - Z_{pp}} \frac{\ln(\Lambda_h/\Lambda_p)}{1 - \Lambda_p/\Lambda_h} \frac{\epsilon_h}{E} \phi_p^0, \quad (2.6)$$

given the effective interaction length $\Lambda_k = \lambda_k^{\text{int}}/(1 - Z_{kk})$. The proton–proton and proton–deuterium total inclusive cross sections per nucleon are quite similar to each other. Charm hadron production is largely independent of whether the interacting particles are protons or neutrons. The cosmic ray flux as a function of energy per nucleon depends on the cosmic ray mass composition. For these reasons, we have denoted the cosmic ray nucleons with p in the Z -moments to evaluate the prompt atmospheric lepton flux.

The high-energy and low-energy regimes are separated by $\epsilon_k \simeq (m_k c^2 h_0 / c\tau_k)$, the critical energy for each hadron k . The hadron k decays dominantly in the low energy regime ($E \ll \epsilon_k$), while it tends to interact at energies higher than ϵ_k . In the end, the resulting neutrino fluxes for each neutrino flavour can be obtained by

$$\phi_\nu = \sum_h \frac{\phi_{h \rightarrow \nu}^{\text{low}} \phi_{h \rightarrow \nu}^{\text{high}}}{(\phi_{h \rightarrow \nu}^{\text{low}} + \phi_{h \rightarrow \nu}^{\text{high}})}. \quad (2.7)$$

For the $(\nu_e + \bar{\nu}_e)$ and $(\nu_\mu + \bar{\nu}_\mu)$ prompt neutrino fluxes, the contributed hadrons h are heavy-flavour hadrons, predominantly charmed hadrons, i.e., $h_c = D_0, D^+, D_s^+$ and Λ_c^+ and their antiparticles. Their critical energies are in the range of $\epsilon_{h_c} \sim 10^7 - 10^9$ GeV. Most of the neutrino energies of interest here are below $\sim \epsilon_{h_c}$, where eq. (2.5) applies and where the prompt neutrino fluxes are isotropic.

While the Z -moment method relies on approximations as discussed above, including those in eqs. (2.4-2.6), it gives results in agreement with those from more direct methods of determining the atmospheric lepton fluxes. A comparison of atmospheric lepton fluxes from pions and kaons using the Z -moment method with the atmospheric lepton fluxes determined from the step-wise solution of the Matrix Cascade Equation (MCEQ) method shows agreement of these predictions to within 5-20%, depending on the zenith angle [50]. In ref. [51], the atmospheric lepton fluxes from the Z -moment method and from a Monte Carlo simulation of the showers that also included charm contributions are shown to be in agreement to within $\sim 20\%$.

2.2 Cosmic ray spectrum

For the cosmic ray all-nucleon fluxes as a function of the energy per nucleon E , there are several parameterizations. A convenient parameterization for comparisons is a broken power law (BPL) spectrum,

$$\phi_p^0(E) [\text{cm}^{-2} \text{s}^{-1} \text{sr}^{-1} (\text{GeV}/A)^{-1}] = \begin{cases} 1.7 E^{-2.7} & \text{for } E < 5 \cdot 10^6 \text{ GeV} \\ 174 E^{-3} & \text{for } E > 5 \cdot 10^6 \text{ GeV}. \end{cases} \quad (2.8)$$

While the BPL approximates the all-particle cosmic ray spectrum, it well approximates the all-nucleon energy spectrum only if the cosmic ray composition consist of only nucleons (or protons). Recent parameterizations of the cosmic ray nucleon spectrum take into account different sources and compositions. Currently, the ultra-high-energy composition of cosmic rays is not clearly identified (see, e.g., ref. [52] for a review). Although the origin of cosmic rays, together with the composition, is still a topic of intense debate, two models frequently used, referred as H3p and H3a, involve three possible cosmic ray source components: supernova remnants, other galactic sources and extra-galactic sources [53]. The difference between the two spectrum models is the component of high-energy cosmic rays originated from the extra-galactic sources, only protons for H3p and a mixed composition, also involving heavier nuclei, for H3a. It is also worth mentioning that the most recent estimates from cosmic ray extended air shower experiments, such as the Pierre Auger Observatory [54] and Telescope Array [55], point towards a mixed composition at the highest energies (see also refs. [52, 56]).

Although the BPL is based on over-simplified assumptions, it is commonly used for comparisons with other existing evaluations. In this work, we use the BPL as the reference cosmic ray nucleon spectrum to evaluate and illustrate which ranges of \sqrt{s} of cosmic ray nucleon interactions with air nucleons, and which ranges of charmed-meson hadron-collider (i.e. nucleon-nucleon center-of-mass) rapidities, play the most relevant role in determining the prompt atmospheric neutrino fluxes at different neutrino energies. We also evaluate the prompt neutrino fluxes with the H3p and H3a spectra and compare the latter with the predictions obtained using the BPL spectrum.

3 Z -moments and atmospheric neutrino fluxes from charm

3.1 Z -moments for charm hadron production

As discussed in the previous section, atmospheric neutrino fluxes can be obtained in terms of Z -moments: Z_{pp} for proton regeneration, Z_{ph} and Z_{hh} for hadron production and regeneration, and $Z_{h\nu}$ for decays to neutrinos (see eqs. (2.5) and (2.6)). We use standard inputs for Z_{pp} and Z_{hh} . While the evaluation of $Z_{h\nu}$ is relatively straightforward, there are large uncertainties in the Z -moments for the production of heavy-flavour hadrons (Z_{ph}), and consequently in the prediction of prompt neutrino fluxes.

The uncertainty in theoretical predictions of the Z_{ph} 's mainly come from the truncation of the QCD perturbative expansion for differential cross sections of heavy-flavour production at

next-to-leading order (NLO) [42, 43]. The QCD scale dependence through the renormalization scale (μ_R) and factorization scale (μ_F) is particularly large for charm production, also due to the smallness of the charm quark mass, well above Λ_{QCD} to allow for the application of a perturbative treatment, but still close enough to it to lead to relatively large $\alpha_s(\mu_R)$ values and to the evaluation of parton distribution functions at characteristic scales μ_F close to the lowest extremes of their characteristic range of evolution. We mitigate this uncertainty by anchoring our prediction to LHCb data on open charm production for collider rapidities of charm hadrons in the range $2 \leq y \leq 4.5$ [44–46]. We evaluate charm production in the collider frame (proton-proton center of mass frame CM), then boost to the fixed-target frame to calculate the Z -moments. Rapidities change under boosts from collider frame to fixed-target frame by $\Delta y = \tanh^{-1}\beta \simeq \ln(\sqrt{s}/m_p)$, so that the CM charm hadron y can be easily converted to the fixed-target frame. Since we focus here on connections to LHC experiments, we only reference CM rapidities in case of charm hadrons.

In our previous works for estimating the prompt neutrino fluxes generated at the LHC [15–17], we evaluated the differential cross sections for charm meson production including NLO QCD corrections in a 3-flavour number scheme framework and compared with the LHCb data. In ref. [16], in particular, we used the PROSA 2019 PDFs fitted in this same fixed flavour number scheme (FFNS) [35] and found that the QCD scales of $(\mu_R, \mu_F) = (1, 2) m_T$ with the transverse mass $m_T = (p_T^2 + m_c^2)^{1/2}$, and the intrinsic transverse momentum smearing $\langle k_T \rangle = 1.2$ GeV yielded results that are reasonably well-matched to the LHCb data. In this work, we use this parameter set and focus on the PROSA FFNS PDFs as default inputs in evaluating theoretical predictions on the prompt atmospheric neutrino flux.

Most of the contributions to the cross sections for charmed hadron production in hadron collisions at high energies come from gluon interactions. Figure 1 shows the ratio of the gluon distribution functions $xg(x, Q^2)$ to the same quantity using the best fit of the PROSA PDF set for $Q^2 = 10$ GeV². The uncertainty from the 40 variations within the PROSA PDF set is presented with the orange band, and the central fits of other 3-flavour NLO PDFs, i.e. CT14 [57], ABMP16 [58], NNPDF3.1 [59] and NNPDF4.0 [60], are also shown for comparison. The experimental data involved in the determination of existing PDFs cover a limited x region, mainly $10^{-4} \lesssim x \lesssim 10^{-1}$ from ep deep inelastic scattering (DIS) at HERA and $x \gtrsim 10^{-5}$ from pp scattering at the LHC [3]. Large uncertainties remain for $x \gtrsim 0.6$. Due to combination of a lack of coverage of the x range and insufficient data, the PDFs are currently not well constrained for both the very low- x and the large- x regions, which leads to the large uncertainty band as indicated in the figure.

The NNPDF4.0 NLO set is an outlier in these comparisons. This new set differs from the NNPDF3.1 in its machine learning methodology and the addition of 44 new data sets [60]. The data sets on inclusive jet, dijet and $t\bar{t}$ production play a role in determining the gluon distribution. These processes are better described by NNLO calculations than by NLO calculations, so the NLO fit to these data is less reliable than the NNLO fit.

Figure 2 shows the differential cross sections for charm meson production $d\sigma/dx_h$ evaluated using the best fits of the different PDFs shown in Fig. 1. We present the predictions

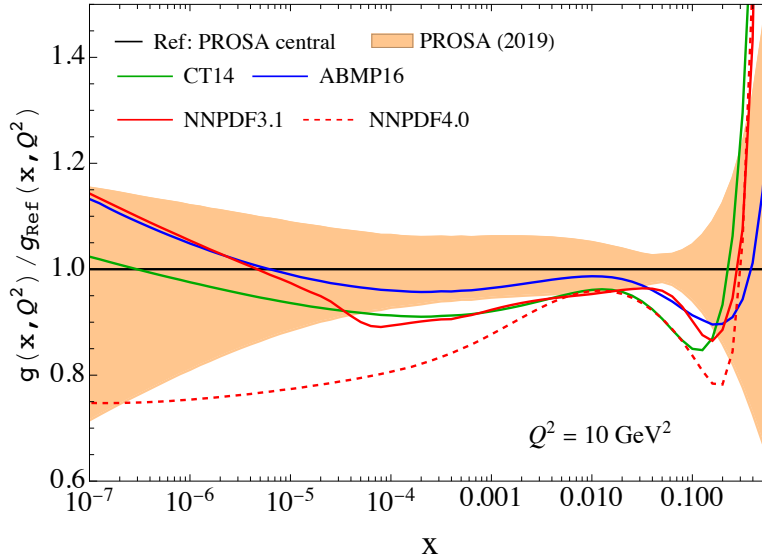


Figure 1. Gluon distribution function uncertainty for $Q^2 = 10 \text{ GeV}^2$ evaluated using the 40 different eigenvectors in the PROSA PDF set (orange band), normalized to the best fit of the PROSA FFNS (2019) PDF set [35]. The uncertainty band is determined from the appropriate combination of fit, model and parameterization uncertainties following the PROSA prescription (see, e.g., Appendix A of ref. [16]). The ratios of the central NLO gluon distributions in the same flavour number scheme by CT14 [57] (green), ABMP16 [58] (blue), NNPDF3.1 [59] (red) and NNPDF4.0 [60] (red dashed) to the PROSA best fit are also shown.

for the D^0 meson for $E_p = 10^6 \text{ GeV}$ and 10^8 GeV as representatives, and multiply by a factor of 2 to account for both D^0 and \bar{D}^0 production since there is equal production of c and \bar{c} in our calculation, and we implement fragmentation with the Peterson fragmentation functions [61]. However, we note that there are some indications of meson/antimeson production asymmetries at LHCb [62, 63], to be better investigated with forthcoming higher-statistics data. In the evaluation, to approximate the production in p -Air collisions, the cross sections for hadron production in pp collisions are scaled by the average atomic number $\langle A \rangle = 14.5$ of air. The variable x_h is the energy fraction of the produced hadron, $x_h \equiv E_h/E_p$.

The charm mesons from cosmic ray interactions in the atmosphere are produced in the forward direction. In this case, the momentum fractions of the partons involved in the interactions from the two sides have typically very different values: the parton momentum fraction from the incident cosmic ray (x_1) is large, whereas the one from the target nucleus in the air nucleus (x_2) is very small. More specifically, while the former (x_1) is approximated to x_h , the latter (x_2) can be as small as $\mathcal{O}(10^{-6})$ when $E_p = 10^8 \text{ GeV}$ and even smaller for higher incident cosmic ray nucleon energies. As discussed above and shown in Fig. 1, in such low- x regions as well as for $x \gtrsim 0.1$, the PDFs are not well constrained by the experimental data. This is indicated in Fig. 2, in which one can see that the difference between the predictions evaluated with the different central PDF sets becomes larger as x_h increases, due to the

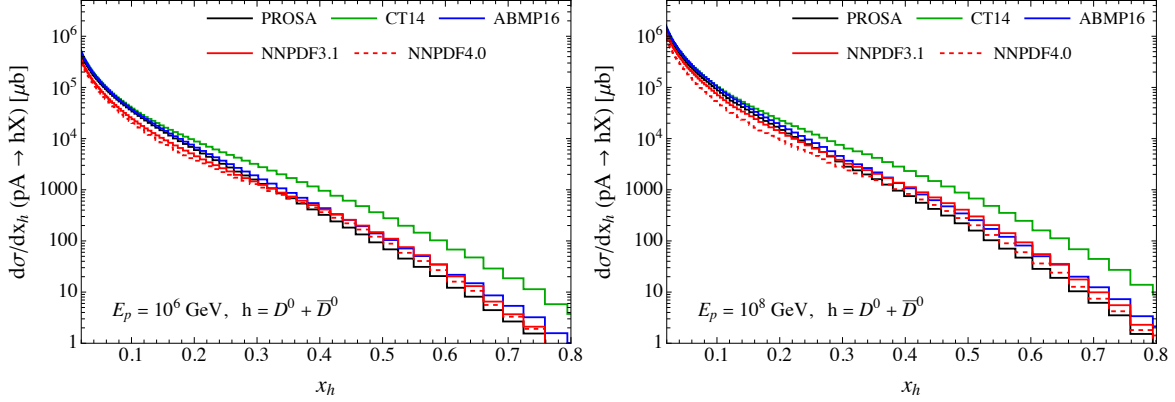


Figure 2. The differential cross section for the sum of D^0 plus \bar{D}^0 production in p -Air collision, $d\sigma/dx_h$ as a function of $x_h = E_h/E_p$ for $E_p = 10^6$ GeV and 10^8 GeV evaluated with the central 3-flavour NLO PDF sets from the PROSA [35], CT14 [57], ABMP16 [58], NNPDF3.1 [59] and NNPDF4.0 [60] groups.

combined effects of low- x and large- x PDF behaviour.

The Z -moment for hadron production in eq. (2.3) and (2.2) can be expressed in terms of the momentum fraction x_h as

$$Z_{ph}(E_h) = \int_0^1 \frac{dx_h}{x_h} \frac{\phi_p^0(E_h/x_h)}{\phi_p^0(E_h)} \frac{1}{\sigma_{pA}(E_h)} \frac{d\sigma(pA \rightarrow hX)}{dx_h}. \quad (3.1)$$

One of goals of this work is to investigate the impact and the range of collider kinematic variables for the predictions of the prompt atmospheric neutrino fluxes. As mentioned earlier in the Introduction, a center of mass (CM) energy of $\sqrt{s} = 14$ TeV, foreseen for HL-LHC, corresponds to $E_p \sim 10^8$ GeV in the fixed-target frame. The next-generation collider FCC aims to increase the energy up to $\sqrt{s} = 100$ TeV, equivalent to $E_p \sim 5 \times 10^9$ GeV in the fixed-target frame. The energy range relevant for probing prompt atmospheric neutrinos is $10^5 \lesssim E_\nu/\text{GeV} \lesssim 10^8$. Neutrino with energies greater than 10^7 GeV are typically produced by pp interactions with $\sqrt{s} > 14$ TeV, as we will show in the next section. Measurements of the heavy-flavour production at the LHC and the FCC will provide useful information for better predictions of the prompt atmospheric neutrino fluxes. Here, to relate to collider variables in a more straightforward way, we first convert the expression in eq. (3.1) into integration over the CM collision energy \sqrt{s} , converting the $x_h = E_h/E_p$ limits of x_h varying between 0 and 1 to limits on \sqrt{s} , varying between $\sqrt{s}_{\min} = \sqrt{2m_p E_h}$ and ∞ , by writing

$$Z_{ph}(E_h) = \int_{\sqrt{s}_{\min}}^{\infty} \frac{d\sqrt{s}}{\sqrt{s}/2} \frac{\phi_p^0(s/2m_p)}{\phi_p^0(E_h)} \frac{d\sigma(pA \rightarrow hX; E_p = \frac{s}{2m_p}, x_h = \frac{2m_p E_h}{s})}{\sigma_{pA}(E_h) dx_h}. \quad (3.2)$$

We show the differential Z -moments for $D^0 + \bar{D}^0$ production as a function of both the center-of-mass energy \sqrt{s} and the energy of the produced charm mesons E_D in Fig. 3. We present the predictions for $D^0 + \bar{D}^0$ production as representative of also other charmed-meson species,

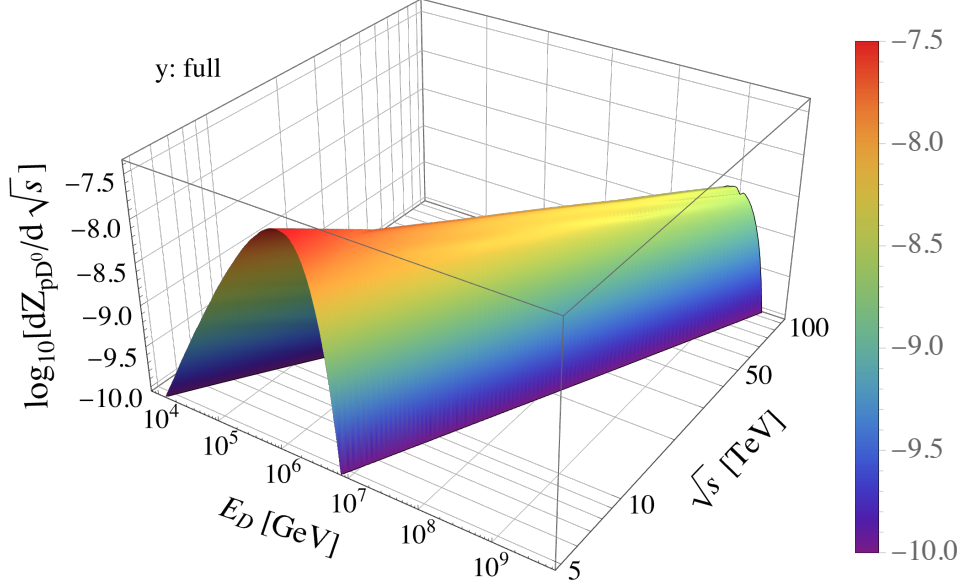


Figure 3. Distribution of differential Z -moment for $D^0 + \bar{D}^0$ production in proton-air collisions as a function of both the center-of-mass collision energy \sqrt{s} and the D^0 (\bar{D}^0) meson energy. The broken power law spectrum is used as input for the cosmic ray flux.

for illustration purposes. In the evaluation, the broken power-law spectrum in eq. (2.8) is used as input for incident cosmic ray flux. For a given E_D , Fig. 3 shows the range of \sqrt{s} values that contribute to $Z_{pD^0}(E_D)$, which increases to higher center-of-mass collision energy with increasing E_D .

The left panel of Fig. 4 shows the impact of the range of \sqrt{s} in eq. (3.2), on the Z -moments for $D^0 + \bar{D}^0$ meson production as a function of the D^0 (\bar{D}^0) meson energy for $\sqrt{s}_{\max} = 7, 14$ and 100 TeV, and for the full range of \sqrt{s} . The first two cuts on the collision energy are to show the reach in E_D of Run 1 and HL-LHC, respectively (the maximum reach of Run 2 and Run 3, not shown explicitly in the plot, are indeed between the previous ones). The potential \sqrt{s} reach of the FCC is $\sqrt{s}_{\max} = 100$ TeV. One can see that the Z_{pD^0} -moment evaluated by integrating over CM energies up to a maximum value of 14 TeV is sizable for E_D smaller than 10^7 GeV, while the cross sections for charmed hadron production with center-of-mass energies up to $\sqrt{s}_{\max} = 100$ TeV contribute to most of the Z -moments for higher E_D .

In the right panel of Fig. 4, we show the Z -moments for the $D^0 + \bar{D}^0$ produced in different ranges of CM charm hadron rapidity y using the results integrated over the full range of \sqrt{s} . Of course, in colliders, charm mesons can be produced in both forward and backward directions. Since we use the collider rapidity, the prediction denoted as ‘ y : full’ includes both positive and negative values of charm hadron CM y . We denote charm hadron rapidity in the fixed-target frame with y^{fixed} . Charm hadrons with both negative y and large $|y|$ in the collider frame translate to low energies in the fixed target frame since $y^{\text{fixed}} \simeq y + \ln(\sqrt{s}/m_p)$

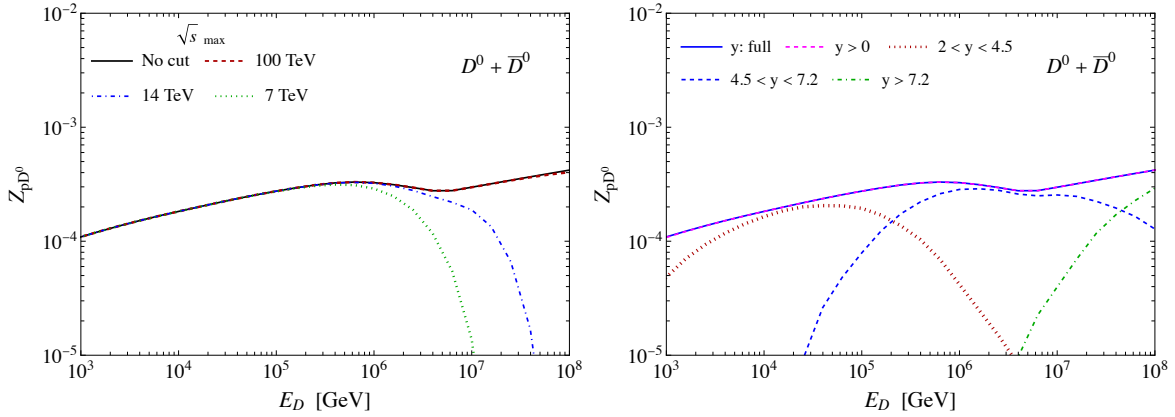


Figure 4. The production moment Z_{pD^0} for $D^0 + \bar{D}^0$ in proton-Air collisions with a broken power law cosmic ray spectrum, evaluated for different values of the maximum hadronic collision energy \sqrt{s}_{\max} (left) and charm hadron CM rapidity ranges (right).

as noted above.

The prediction with collider frame charm hadron rapidity $y > 0$ is smaller than the full prediction by $\sim 10\%$ at $E_D = 10^2$ GeV, while they overlap for the energies presented in the figure. Thus, for the energies relevant to the prompt atmospheric neutrino fluxes, the Z -moments can be described by charm mesons produced in the forward direction in the collider frame ($y > 0$). We separate further the charm hadron collider frame rapidity range into three parts, $2 < y < 4.5$, $4.5 < y < 7.2$ and $y > 7.2$. The range of charm hadron rapidity $2 < y < 4.5$ is covered by the LHCb experiment. This range is the most forward region for heavy-flavour production probed to date at the LHC.

3.2 Z -moments and FPF neutrinos

The forward neutrino experiments at the LHC investigate the region of $\eta_\nu > 7.2$. The neutrino rapidity is correlated with the charm hadron rapidity, as shown in the left panel of Fig. 5. The left panel shows $(1/\sigma)d\sigma/d\eta_\nu$ for the $\nu_\mu + \bar{\nu}_\mu$ that come from decays of D^0 and \bar{D}^0 produced in hadron rapidity ranges 4.75 – 5.25 (blue), 5.75 – 6.25 (orange), 6.75 – 7.25 (green) and $y > 7.25$ (purple). The cross section normalized distributions show spreads in η_ν centered around a narrow range of charm hadron y . The right panel of Fig. 5, where absolute distributions are depicted, shows that in addition to the spread in η_ν relative to the parent charm hadron rapidities, the fact that $d\sigma/d\eta_\nu$ falls quickly as η_ν increases means that for $\eta_\nu > 8$, a nearly equal number of muon neutrinos from D^0 decays come from D^0 's with $y > 7.25$ and with y in the range 6.75 – 7.25 for $\sqrt{s} = 14$ TeV.

Figure 6 shows the muon neutrino and antineutrino pseudorapidity distributions from the D^0 and \bar{D}^0 produced in the rapidity ranges 2 – 4.5, 4.5 – 7.2 and greater than 7.2, as well as the sum ($y > 2$), at a pp collider with $\sqrt{s} = 14$ TeV (left) and $\sqrt{s} = 100$ TeV (right). The left panel of Fig. 6 shows that the portion of $d\sigma/d\eta_\nu$ coming from the charm hadron rapidity

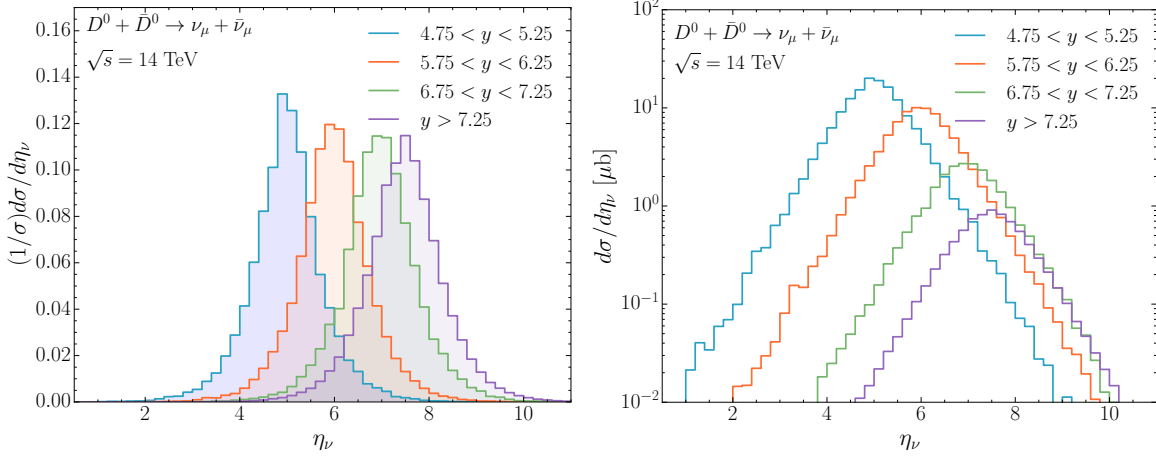


Figure 5. The cross-section normalized muon neutrino pseudorapidity distribution $(1/\sigma)d\sigma/d\eta_\nu$ (left) and the absolute muon neutrino pseudorapidity distribution $d\sigma/d\eta_\nu$ (right) for $pp \rightarrow D^0 + \bar{D}^0 \rightarrow \nu_\mu + \bar{\nu}_\mu$ production from parent charm hadrons in rapidity ranges $4.75 - 5.25$, $5.75 - 6.25$, $6.75 - 7.25$ and for rapidity larger than 7.25 . Note the different scales on the vertical axis.

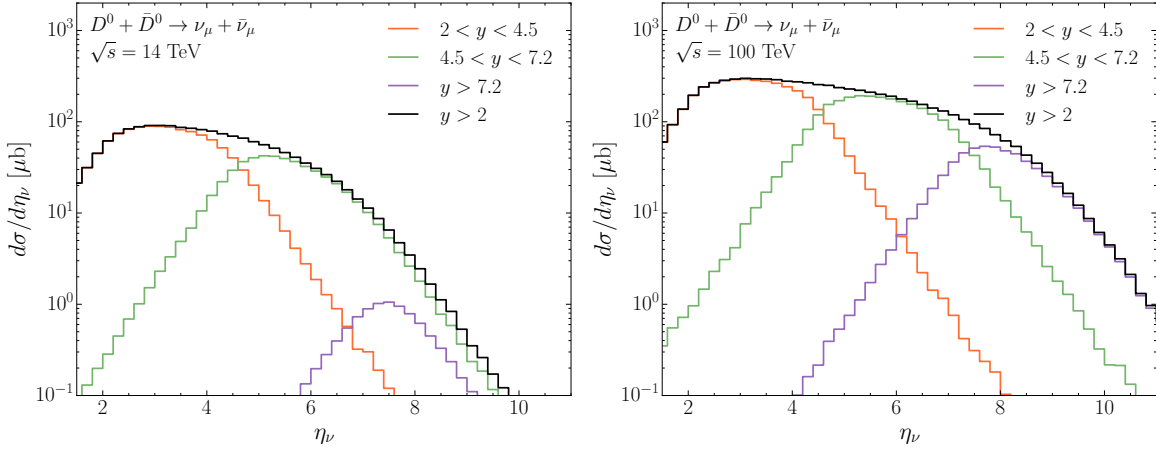


Figure 6. The $\nu_\mu + \bar{\nu}_\mu$ pseudorapidity distribution from decays of $D^0 + \bar{D}^0$ produced in the rapidity ranges $2 < y < 4.5$, $4.5 < y < 7.2$, $y > 7.2$ and for $y > 2$ in pp collisions at $\sqrt{s} = 14$ TeV (left) and $\sqrt{s} = 100$ TeV (right).

range $4.5 < y < 7.2$ is actually larger than the one from $y > 7.2$ at the LHC with $\sqrt{s} = 14$ TeV. The ratio of the green histogram ($4.5 < y < 7.2$) to the purple histogram ($y > 7.2$) is ~ 2.9 for $\eta_\nu = 8$ and ~ 2.1 for $\eta_\nu = 9$. This means that experiments at the Forward Physics Facility that measure neutrinos with $\eta_\nu > 7.2$ will be sensitive to the rapidity range of charm meson production that is important for the prompt atmospheric neutrino fluxes in the $\sim 10^6$ GeV energy range.

The right panel of Fig. 6 shows that for $\sqrt{s} = 100$ TeV, the neutrino pseudorapidity distribution for $\eta_\nu \gtrsim 8$ is dominated by the decay of $(D^0 + \bar{D}^0)$ produced with $y > 7.2$,

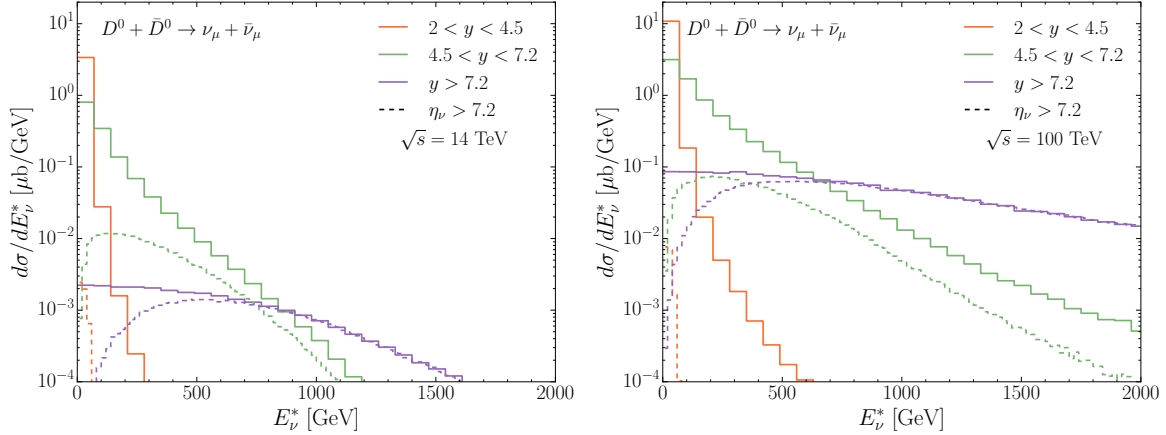


Figure 7. The $\nu_\mu + \bar{\nu}_\mu$ collider energy (E_ν^*) distribution from D^0 and \bar{D}^0 in the rapidity ranges $2 < y < 4.5$, $4.5 < y < 7.2$ and for $y > 7.2$ in case of pp collisions at $\sqrt{s} = 14$ TeV (left) and $\sqrt{s} = 100$ TeV (right). The solid histograms show E_ν^* distributions in the collider frame for all η_ν , whereas all the dashed histograms show the energy distributions from the corresponding charm meson y intervals that give neutrinos and antineutrinos with $\eta_\nu > 7.2$, corresponding to the acceptance of detectors at the FPF.

whose contribution is much larger than the one from $(D^0 + \bar{D}^0)$ with $4.5 < y < 7.2$. For example, one can see that the purple histogram is a factor of $\sim 3.5(11)$ larger than the green histogram for $\eta_\nu = 8(9)$.

To complete the discussion of the relation between the kinematical properties of D^0 and \bar{D}^0 at the LHC and the rapidities of neutrinos from charm in the prompt atmospheric neutrino fluxes, Fig. 7 shows the collider frame energy (E_ν^*) distributions of neutrinos from $D^0 + \bar{D}^0$ in the rapidity ranges $2 < y < 4.5$, $4.5 < y < 7.2$ and for $y > 7.2$ in case of pp collisions at $\sqrt{s} = 14$ TeV (left) and $\sqrt{s} = 100$ TeV (right). The solid histograms show the neutrino energy distributions including all values of η_ν . The dashed histograms show the energy distributions of neutrinos with $\eta_\nu > 7.2$ from each of the aforementioned $D^0 + \bar{D}^0$ rapidity ranges. The dashed histogram in the left panel shows that for charm hadron rapidity $4.5 < y < 7.2$, a substantial fraction of the neutrinos with energies above a few hundred GeV have $\eta_\nu > 7.2$ (representative of an FPF detector coverage) for $\sqrt{s} = 14$ TeV. We note that the $\nu_\mu + \bar{\nu}_\mu$ energy distribution from $D^0 + \bar{D}^0$ essentially equals the $\nu_e + \bar{\nu}_e$ energy distribution from $D^0 + \bar{D}^0$. We also notice that the FPF detectors will be sensitive to a wide energy range, from E_ν^* of order tens of GeV to E_ν^* of the order of a few TeV. The $\nu_e + \bar{\nu}_e$ flux at the FPF is dominated by charm production and decay at high energy. In the 100's of GeV neutrino energy range, it will be important to disentangle the charm contribution from the kaon contribution to this flux.

With $\sqrt{s} = 14$ TeV, corresponding to a proton beam energy in the fixed-target frame is $\sim 10^8$ GeV, the highest energy collider neutrinos with $\eta_\nu > 7.2$ come from charm hadrons produced with $y > 7.2$, whereas at lower E_ν^* they come predominantly from hadrons produced

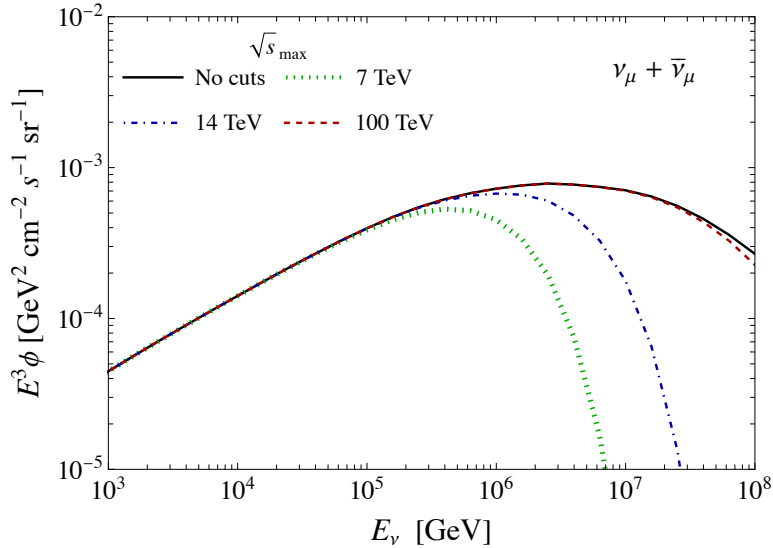


Figure 8. The prompt flux of atmospheric $\nu_\mu + \bar{\nu}_\mu$ for collision energies \sqrt{s} varying up to different values of a maximum \sqrt{s}_{max} .

with $y < 7.2$ as shown in the left panel Fig. 7. The right panel of Fig. 7 shows that for $\sqrt{s} = 100$ TeV, corresponding to a proton energy in the fixed target frame of $\sim 5 \times 10^9$ GeV, there is a qualitatively similar behavior, but with an E_ν^* crossover point shifted to a lower value.

3.3 Atmospheric neutrino fluxes from charm hadrons

The resulting $\nu_\mu + \bar{\nu}_\mu$ fluxes of atmospheric neutrinos from the prompt decays of charm hadrons, scaled by E_ν^3 , are shown in Figs. 8 and 9. We include contributions from the decays of D^0 , D^+ , D_s^+ and Λ_c^+ and their antiparticles. For prompt neutrinos, the flux of $\nu_\mu + \bar{\nu}_\mu$ is essentially equal to that of $\nu_e + \bar{\nu}_e$ and is isotropic up to energies $E_\nu \sim 10^7$ GeV. Shown in Figs. 8 and 9 are the fluxes in vertical direction.

In Fig. 8, the predictions evaluated for different values of the maximum hadronic collision energy \sqrt{s}_{max} are presented, as in the left panel of Fig. 4 for the Z_{pD^0} . As with the Z -moment, appreciable contributions to the prompt neutrino flux evaluated with $\sqrt{s} \leq 14$ TeV appear below 10 PeV, in agreement with the findings of a previous study published in Ref. [64]. The energies of produced neutrinos are lower than those of their parent particles, with the parent particle fluxes determined with $Z_{ph}(\sqrt{s} < \sqrt{s}_{\text{max}})$. The neutrino flux obtained under the cut $\sqrt{s}_{\text{max}} = 14$ TeV accounts for 93% and 25% of the total flux evaluated with the whole range of CM hadronic collision energies (no cuts) at $E_\nu = 10^6$ GeV and 10^7 GeV, respectively, while the same cuts on \sqrt{s}_{max} yield 99% and 63% of contributions to Z_{pD^0} at the corresponding energies. Considering that the prompt atmospheric neutrino flux is dominant over the conventional atmospheric neutrino flux above $E_\nu = 10^5 - 10^6$ GeV, the study of charm hadron production at the LHC will be able to constrain the prompt atmospheric neutrino

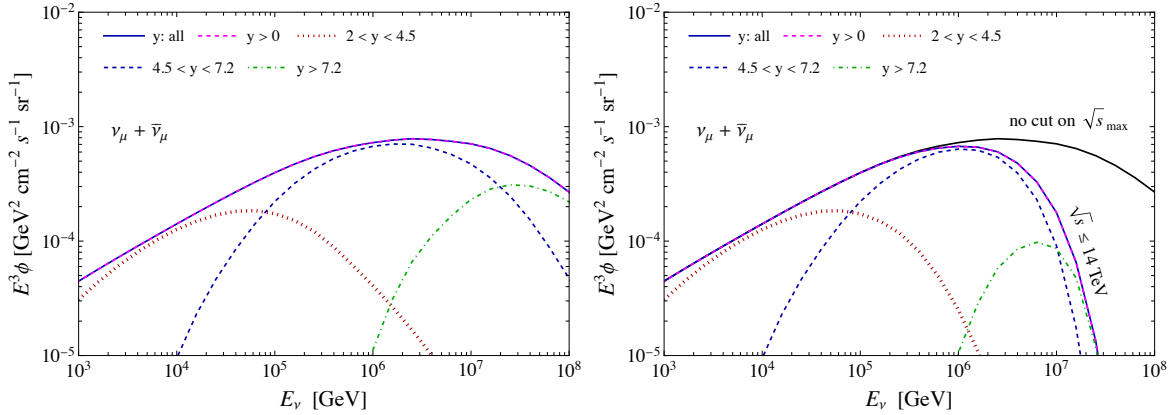


Figure 9. The prompt flux of atmospheric $\nu_\mu + \bar{\nu}_\mu$ from different charm hadron collider-frame rapidity ranges in $pp \rightarrow c\bar{c}X$, using a broken power law cosmic ray spectrum. The left panel includes the fluxes evaluated without cuts on \sqrt{s}_{\max} , whereas the contributions in different rapidity ranges in the right panel are obtained under the condition $\sqrt{s}_{\max} = 14$ TeV.

flux in this energy range and up to $E_\nu \lesssim 10^7$ GeV. On the other hand, as expected from Fig. 8, the charm hadrons produced at $\sqrt{s} \leq 100$ TeV impact the full neutrino energy range most relevant for IceCube [29] and IceCube-Gen2 [65] sensitivity to the prompt atmospheric neutrino component. This means that the FCC will be able to further improve the theoretical predictions of the high energy prompt neutrino fluxes.

In Fig. 9, we show the atmospheric fluxes of $\nu_\mu + \bar{\nu}_\mu$ arising from charm mesons produced in different center-of-mass rapidity ranges. The predictions in the left panel are evaluated with full range of \sqrt{s} , while the ones in the right panel are obtained under the cut $\sqrt{s} \leq 14$ TeV. The predictions in Fig. 9 indicate that the prompt atmospheric neutrinos at the energies $E_\nu \gtrsim 10^5$ GeV, where their flux is important relative to the conventional atmospheric and the diffuse astrophysical neutrino fluxes, come mainly from charm hadrons produced with CM rapidities in the range of $y \gtrsim 4.5$.

The LHC Run 3 forward neutrino experiments SND@LHC and FASER ν cover the pseudo-rapidities $7.2 < \eta_\nu < 8.6$ and $\eta_\nu \gtrsim 8.5$, respectively [25, 66]. The Forward Physics Facility at the HL-LHC is foreseen to host three neutrino detectors, i.e. the Advanced SND (AdvSND) FAR detector, FASER ν 2 and FLArE, with the respective coverage of $7.2 < \eta_\nu < 9.2$, $\eta_\nu \gtrsim 8.5$ and $\eta_\nu \gtrsim 7.5$ [25]. These detectors are still under design, so there is the possibility to cover other pseudo-rapidity ranges. On the other hand, the AdvSND NEAR detector, located in another area of LHC, will cover $4 < \eta_\nu < 5$. We have shown in Fig. 6 that for $\sqrt{s} = 14$ TeV, charm hadrons produced in the range $4.5 < y < 7.2$ yield neutrinos with $\eta_\nu > 7.2$. Thus, all of the forward neutrino experiments at the LHC are sensitive to the kinematic regions relevant for the prompt atmospheric neutrino flux for $E_\nu \gtrsim 10^5$ GeV.

For reference, we also evaluated the atmospheric neutrino flux from charm hadrons that come from CM rapidity $y > 8.5$, namely, neutrinos from charm hadrons that when produced

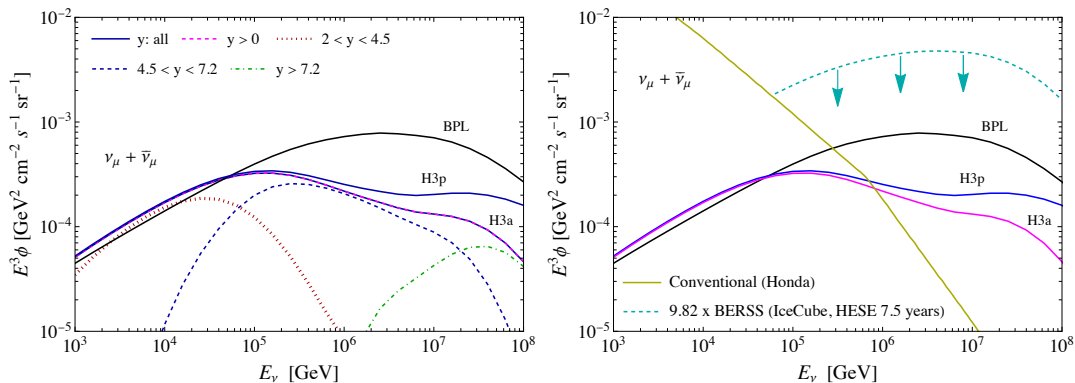


Figure 10. Left: The prompt flux of atmospheric $\nu_\mu + \bar{\nu}_\mu$ from different charm meson CM rapidity ranges in $pp \rightarrow c\bar{c}X$ using the H3p and H3a spectra as well as the broken power law spectrum for cosmic ray fluxes. Right: The prompt flux of atmospheric $\nu_\mu + \bar{\nu}_\mu$ from H3p, H3a and BPL cosmic ray spectra is shown with the vertical conventional $\nu_\mu + \bar{\nu}_\mu$ flux [67] and the IceCube upper limit on the prompt atmospheric flux [29], expressed as a scaling of the BPL flux from ref. [38].

in the collider have momenta that point in the direction of the FASER ν /FASER ν 2 detectors. For the atmospheric neutrino fluxes evaluated with $\sqrt{s}_{\text{max}} = 14$ TeV, the contribution from charm hadron CM rapidities $y > 8.5$ to the total flux is much less than 0.1% at $E_\nu = 10^7$ GeV, therefore completely negligible. Even in case calculated with no cut on \sqrt{s} , the contribution from charm hadrons with CM rapidity $y > 8.5$ is less than 1% at $E_\nu = 10^7$ GeV, and at most $\sim 20\%$ at $E_\nu = 10^8$ GeV.

Thus far, we have used the BPL cosmic ray spectrum to illustrate the impact of hadronic collisions at different \sqrt{s} and charmed mesons produced in different CM rapidities on the prompt atmospheric neutrino flux. For reference, the left panel of Fig. 10 presents the prompt fluxes of atmospheric $\nu_\mu + \bar{\nu}_\mu$ evaluated also with the H3p and H3a cosmic ray spectra. Similarly to the left panel of Fig. 9, the contributions from the different charm hadron CM rapidity ranges are presented for the predictions evaluated with the H3a cosmic ray spectrum. The conclusions are similar to those already drawn when analyzing the BPL case.

The right panel of Fig. 10 shows the vertical prompt atmospheric $\nu_\mu + \bar{\nu}_\mu$ fluxes along with the vertical conventional atmospheric neutrino flux [67] and the IceCube Collaboration's 90% upper limit on the prompt $\nu_\mu + \bar{\nu}_\mu$ flux from the analysis of high energy starting events (HESE) collected in 7.5 years [29]. The upper limit is represented by a scaling of the BERSS prediction [38].

4 Uncertainty from the parton distribution functions

As discussed in the previous section, for neutrinos produced in forward region, the colliding partons in the interaction have asymmetric longitudinal momentum fractions (x). High energy neutrinos from charm produced in interactions of cosmic rays with a steeply-falling energy spectrum favor a momentum fraction from cosmic rays that is large while the momentum

fraction of the parton in the struck air nucleon is very small. At the CM energies relevant for this work, the respective values of x can be larger than 0.1 and less than 10^{-5} . The PDFs in such regions have been poorly constrained due to lack of experimental data or of experimental data precise enough. Prompt neutrino flux at higher energies are affected by PDF at decreasing x values. For $E_\nu \gtrsim 10^6$ GeV, the contribution of collisions with gluons in the nucleon target with $x < 10^{-5}$ is significant. At higher energies, the lower x region become more important, which is reflected in Fig. 11. On the other hand, the effect of variations in the large- x PDFs affects the normalization of the prompt neutrino flux for whole energy range, and the PDFs in the range of $x > 0.6$ have a negligible effect [64].

Using the BPL cosmic ray flux, we illustrate the energy and CM-rapidity dependence of the PDF uncertainties associated with the PROSA PDF fit procedure, theoretical model and parameterizations on the predicted prompt atmospheric neutrino flux. The orange band is the uncertainty envelope determined using the 40 variants in the PROSA PDF fit (see appendix A of ref. [16]). Each of the four panels of Fig. 11 also shows results obtained with central NLO PDFs from the CT14, ABMP16, and NNPDF3.1 fits as well as the newer NNPDF4.0 version. The upper left panel shows the prompt flux and uncertainty band for the full CM-rapidity range relevant for prompt neutrino production, along with the ratio of the predictions with different PDFs to those with the central PROSA PDFs. The three other panels of Fig. 11 show the results for the restricted CM-rapidity ranges of $2 < y < 4.5$, $4.5 < y < 7.2$ and $y > 7.2$.

The results in Fig. 11 show that the overall uncertainty of the PROSA PDF result increases with energy, and it is within +25 % and -35 % around the prediction with the central PROSA fit for $E_\nu \lesssim 10^8$ GeV. The fluxes for $2 < y < 4.5$ dominantly contribute to the total flux below $\sim 10^5$ GeV, where the uncertainty due to the different PROSA PDF sets are within $\pm 10\%$. The LHCb data on heavy-flavour production in this range are included in the PROSA PDF fit [35]. The different sets of the PROSA PDFs yield an uncertainty in the range of +15% and -20% for the fluxes with $4.5 < y < 7.2$, which are dominant for the energy range of 10^5 GeV $\lesssim E_\nu \lesssim 10^7$ GeV. The PROSA PDF uncertainty increase to +25% and -35% at 10^7 GeV for the fluxes from charm hadrons with CM rapidities $y > 7.2$.

In the region where experimental data are not available, the uncertainty from the PROSA PDFs strongly depend on the parameterization chosen, and correspond to an extrapolation, although still constrained by sum rules. Comparing with the results evaluated using the other PDFs considered here, one can see that the fluxes with the CT14 central PDF set are out of the PROSA uncertainty band. The CT14 PDFs yield the largest fluxes with difference of +40 - 60 % with respect to the central prediction with the PROSA PDFs for 10^3 GeV $\leq E_\nu \leq 10^8$ GeV. This is related to the large- x behaviour of the considered PDFs. The ABMP16 central predictions lie almost on the upper boundary of the PROSA uncertainty band in all the rapidity ranges. The evaluations with the NNPDF central PDF sets are mostly lower than the PROSA predictions. For $E_\nu < 10^5$ GeV and $2 < y < 4.5$, both NNPDF3.1 and NNPDF4.0 central predictions are even less than the lower boundary of the PROSA range. While the NNPDF4.0 PDFs yield fluxes that differ from the central predictions of

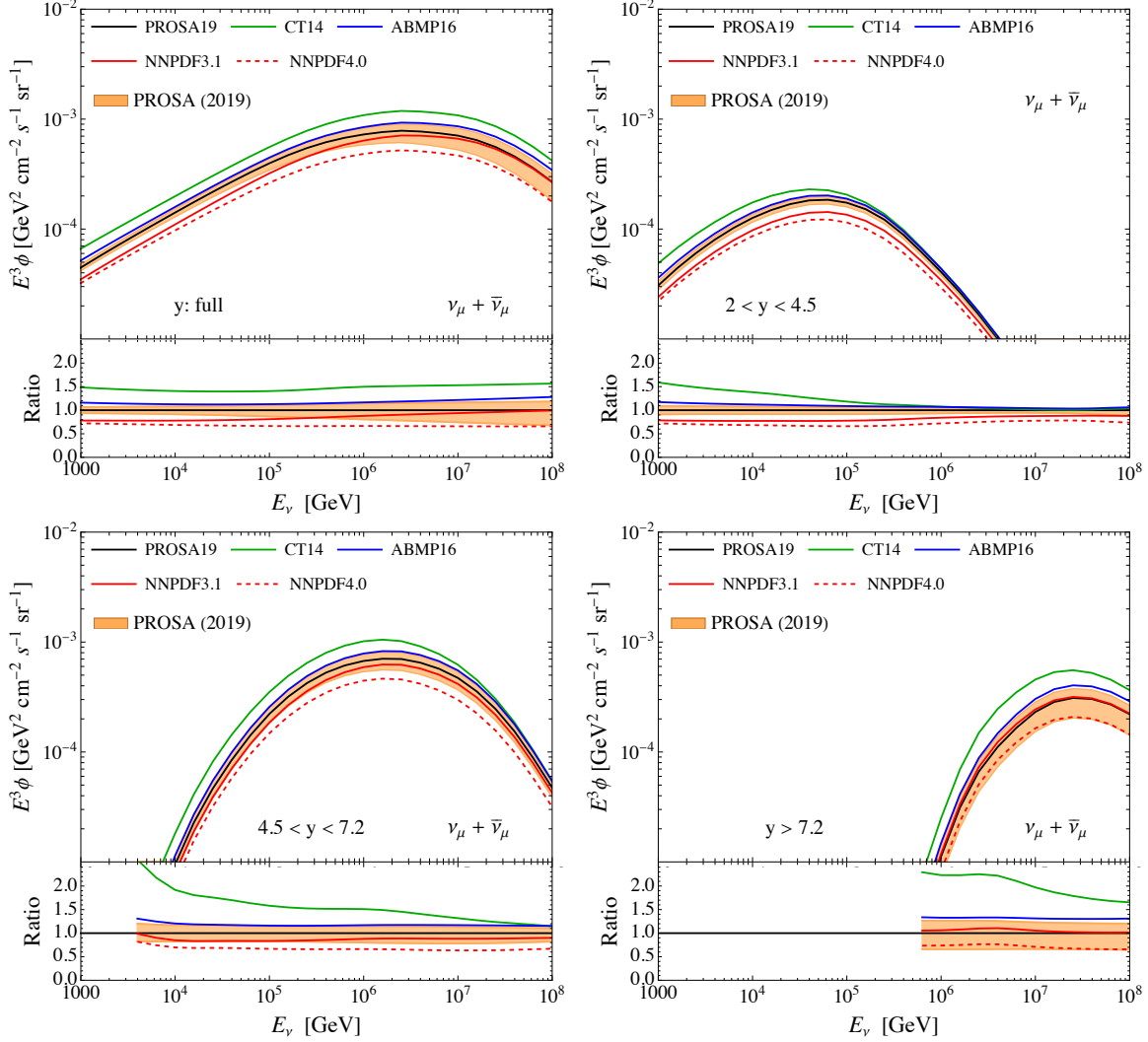


Figure 11. The prompt atmospheric $\nu_\mu + \bar{\nu}_\mu$ fluxes with uncertainties from the 40 eigenvectors of the PROSA 2019 PDF fit and with the central PDFs by other groups presented in Fig. 1. The contributions of neutrinos from charm hadrons in different CM rapidity ranges are shown in different panels. The ratios of predictions to the central PROSA PDFs are presented in the lower part of each panel.

PROSA by about 30 % all over the presented energies, in case of the NNPDF 3.1 PDFs, the discrepancy is reduced as energy increases, and both predictions eventually converge one towards the other at very high energies, i.e. near $E_\nu \sim 10^8$ GeV. This can also be seen in the figures for the different rapidity ranges. For $2 < y < 4.5$, where the contribution to the total fluxes dominate at low energies $E < 10^5$ GeV, both NNPDF central predictions are placed out of the PROSA uncertainty band, but would overlap with it if one would consider the NNPDF uncertainty bands. On the other hand, for $y > 7.2$, which impact the prompt

flux for $E_\nu \sim 10^7$ GeV, the predictions with central NNPDF3.1 and PROSA PDFs turn out to be consistent with each other within 5%.

As outlined at the beginning of Sec. 4, the prompt atmospheric neutrino fluxes are only moderately sensitive to the behaviour of PDFs at very large x ($x \gtrsim 0.6$). On the other hand, as shown in ref. [16], the prompt neutrino flux at the TeV energy scale at the FPF is very sensitive to PDFs at very large x .

5 Discussion and conclusions

In this work, we have investigated relevant kinematic regions for atmospheric prompt neutrino production in terms of \sqrt{s} of the colliding nucleon-nucleon system and the CM rapidity y of the charm hadrons decaying into neutrinos. Our focus includes the energy range from $E_\nu \sim 10^4$ GeV where the conventional atmospheric neutrino flux is larger than the prompt atmospheric neutrino flux, to $E_\nu \sim 10^8$ GeV, where the prompt neutrino flux dominates the conventional neutrino flux and the astrophysical neutrino flux is relevant [27–29]. As shown in Figs. 8 and 9, the LHC \sqrt{s} does not fully cover this neutrino energy range. In fact, the maximum energy of pp collisions at the LHC $\sqrt{s} = 14$ TeV corresponds to $E_p \sim 10^8$ GeV in a fixed-target frame. A fraction of the cosmic ray nucleon energy is transferred to charmed mesons, and neutrinos in turn take just a fraction of the energy of the decaying charmed mesons. As the figures show, prompt atmospheric neutrinos from nucleon-nucleon collisions with center-of-mass energy $\sqrt{s} \leq 14$ TeV are distributed in an energy range up to $E_\nu \lesssim 10^7$ GeV. FCC running in hadron-hadron collision mode with $\sqrt{s} = 100$ TeV would directly connect to prompt atmospheric neutrinos with energies $E_\nu = 10^7$ GeV and higher.

Although the direct correspondence between LHC production of neutrinos from charm and cosmic ray production of neutrinos from charm is limited to atmospheric neutrino energies $\lesssim 10^7$ GeV, this covers the energy ranges where the atmospheric neutrino flux transition from conventional to prompt occurs and the astrophysical flux becomes dominant. LHC forward experiments can play important roles in improving theoretical predictions of prompt atmospheric neutrino fluxes. We showed that the prompt atmospheric neutrino flux for $E_\nu \sim 10^5 - 10^7$ GeV comes mostly from the charm hadrons in the CM rapidity range of $4.5 < y < 7.2$. Although there are not any planned collider experiments capable of direct measurements of distributions of charm hadrons with $y > 7.2$, the range $\eta_\nu > 7.2$ has just started to be probed during the Run 3 at the LHC by the SND@LHC forward neutrino experiment, sensitive to neutrinos from charm (and other) decays (another Run 3 experiment, Faser ν , covers rapidities $\gtrsim 8.5$). This range of η_ν can also be probed during the HL-LHC by the successors of the previous experiments and further new-generation forward experiments in the recently proposed FPF. The key observation here is that, even if a fraction of prompt neutrinos in the range of $\eta_\nu > 7.2$ at the LHC come from charm hadrons with $y > 7.2$, the prompt neutrino fluxes at the FPF experiments are dominated by the decays of charm hadrons with $4.5 < y < 7.2$ as shown in the left panel of Fig. 6, for the neutrino energies shown in the left panel of Fig. 7. The kinematic overlap with the region presently most

interesting for prompt neutrino fluxes emphasizes the deep connection between atmospheric prompt neutrino fluxes and neutrino production from heavy-flavour at the FPF.

At present, there are no direct LHC measurements of charm production in pp collisions beyond the LHCb coverage that extends up to a CM rapidity $y \leq 4.5$. LHCb has presented some analyses in fixed-target modality, but using one of the LHC proton beam on a gaseous nuclear target, such as He and Ar. ALICE is also preparing an upgrade for pA measurements in fixed-target modality, using nuclei different from those considered by LHCb. In fixed-target modality the LHCb-SMOG2 apparatus, active during Run 3, has a collider-frame rapidity coverage $-2.8 < y < 0.2$, whereas the ALICE fixed-target extension at HL-LHC will cover rapidities $-3.6 < y < -2.6$ [68]. These experiments have a nucleon-nucleon \sqrt{s} reach $\mathcal{O}(100)$ GeV, which is of limited interest as for directly probing prompt atmospheric neutrino production, considering the \sqrt{s} relevant for the latter. They are however very useful to probe very large- x PDF behaviour, with impact on the forward high-energy prompt neutrino component at the LHC.

In synergy with existing and forthcoming LHCb measurements of charm hadrons with $2.0 < y < 4.5$, FPF measurements of high-rapidity neutrinos from heavy flavour will help pin down the small- x gluon PDF [24, 25] and possibly reveal signs of saturation effects. The gluon PDF uncertainties are currently a subject of intense discussion, as demonstrated by the fact that the range of predictions of different central PDFs and the PROSA PDF uncertainty band do not fully overlap, as shown in Fig. 11. We emphasize that pinning down PDF uncertainties is not only relevant for reducing the present uncertainties on prompt neutrino fluxes at high energy (see section 4), but also to allow an ambitious precision physics program at the HL-LHC and at future higher-energy hadron colliders.

While not emphasized here, renormalization and factorization scale uncertainties are large for predictions of both the prompt neutrinos at the neutrino experiments of the FPF [15, 16] and of the prompt atmospheric neutrino fluxes [32–39]. The inclusion of higher order QCD corrections will narrow down the scale uncertainties. FPF neutrino measurements at high energies will help testing the robustness of the perturbative QCD description of charm production and the importance of non-perturbative effects.

On the one hand, for prompt atmospheric neutrinos, the focus is on the $\nu_\mu + \bar{\nu}_\mu$ flux (and the essentially equal flux of $\nu_e + \bar{\nu}_e$). The $\nu_\tau + \bar{\nu}_\tau$ atmospheric flux is about an order of magnitude smaller than the $\nu_\mu + \bar{\nu}_\mu$ atmospheric flux [39]. On the other hand, at the FPF, the $\nu_\mu + \bar{\nu}_\mu$ and $\nu_e + \bar{\nu}_e$ fluxes have large contributions from pions and kaons, respectively [18, 25]. However, neutrinos of the highest energies for these two flavours at the FPF have substantial contributions from charm. Additionally, almost all the $\nu_\tau + \bar{\nu}_\tau$ come from prompt charm decays. Tau neutrino and antineutrino measurements at the FPF, in turn, would help untangle charm contributions from pion and kaon contributions to other neutrino flavours. A better understanding of high energy, forward production of pions and kaons will inform modeling of conventional atmospheric neutrino fluxes and of extensive air showers produced by cosmic rays and may resolve outstanding issues associated with the current discrepancy between the number of muons detected and predicted at Earth [69]. At high energies, since

the the prompt diffuse flux of atmospheric muons is nearly equal to the prompt flux of muon neutrinos, even measurements of the atmospheric muon flux [70–72] may be useful to constrain theoretical predictions of neutrino fluxes from charm.

FCC running in hadron-hadron collision mode with $\sqrt{s} = 100$ TeV would directly connect to prompt atmospheric neutrinos with energies $E_\nu = 10^7$ GeV and higher. If the FCC employs experiments that probe the relevant rapidity region for prompt atmospheric neutrino searches (the higher E_ν , the larger are the relevant rapidities, see Fig. 9), it can provide unprecedented information for the prompt flux of atmospheric neutrinos at the highest energies. Measurements at the FCC might be relevant for future generation neutrino telescopes, expected to extend the statistics of high-energy neutrino events for neutrino energies beyond the PeV. On the other hand, importantly, we emphasize that LHC energies are high enough to already probe prompt neutrino production in the current domain of present very large volume neutrino telescopes and in the region where the prompt atmospheric neutrino fluxes are expected to overcome the conventional ones, considering that prompt neutrino production up to $E_\nu \sim \mathcal{O}(\text{PeV})$ is dominated by nucleon-nucleon collisions within LHC maximum \sqrt{s} value. Measurements of prompt neutrinos at forward neutrino experiments at the LHC through Run 3 and HL-LHC stages will shed light on the nucleon structure and will definitely impact the predictions of prompt atmospheric neutrino fluxes.

Acknowledgments

This work is supported in part by U.S. Department of Energy Grant DE-SC-0010113 and DE-SC-0012704 and the National Research Foundation of Korea (NRF) grant funded by the Korea government Ministry of Science and ICT (MSIT) No. 2021R1A2C1009296. The work of M.V.G. is supported in part by the Bundesministerium für Bildung und Forschung under contract 05H21GUCCA.

References

- [1] C. Giunti, J. Gruszko, B. Jones, L. Kaufman, D. Parno and A. Pocar, *Report of the Topical Group on Neutrino Properties for Snowmass 2021*, [2209.03340](#).
- [2] P. Huber et al., *Snowmass Neutrino Frontier Report*, in *2022 Snowmass Summer Study*, 11, 2022 [[2211.08641](#)].
- [3] PARTICLE DATA GROUP collaboration, *Review of Particle Physics*, *PTEP* **2022** (2022) 083C01.
- [4] ICECUBE collaboration, *Measurement of the multi-TeV neutrino cross section with IceCube using Earth absorption*, *Nature* **551** (2017) 596 [[1711.08119](#)].
- [5] M. Bustamante and A. Connolly, *Extracting the Energy-Dependent Neutrino-Nucleon Cross Section above 10 TeV Using IceCube Showers*, *Phys. Rev. Lett.* **122** (2019) 041101 [[1711.11043](#)].
- [6] ICECUBE collaboration, *Determining neutrino oscillation parameters from atmospheric muon neutrino disappearance with three years of IceCube DeepCore data*, *Phys. Rev. D* **91** (2015) 072004 [[1410.7227](#)].

- [7] KM3NET collaboration, *Letter of intent for KM3NeT 2.0*, *J. Phys. G* **43** (2016) 084001 [[1601.07459](#)].
- [8] JUNO collaboration, *Sub-percent Precision Measurement of Neutrino Oscillation Parameters with JUNO*, [2204.13249](#).
- [9] SUPER-KAMIOKANDE collaboration, *Constraints on neutrino oscillations using 1258 days of Super-Kamiokande solar neutrino data*, *Phys. Rev. Lett.* **86** (2001) 5656 [[hep-ex/0103033](#)].
- [10] SNO collaboration, *Direct evidence for neutrino flavor transformation from neutral current interactions in the Sudbury Neutrino Observatory*, *Phys. Rev. Lett.* **89** (2002) 011301 [[nucl-ex/0204008](#)].
- [11] A. De Rujula and R. Ruckl, *Neutrino and muon physics in the collider mode of future accelerators*, in *ECFA-CERN Workshop on large hadron collider in the LEP tunnel, Lausanne and CERN, Geneva, Switzerland, 21-27 Mar 1984: Proceedings. 1.*, pp. 571–596, 1984, [DOI](#).
- [12] K. Winter, *Detection of the tau-neutrino at the LHC*, in *ECFA Large Hadron Collider Workshop, Aachen, Germany, 4-9 Oct 1990: Proceedings.2.*, pp. 37–49, 1990.
- [13] A. De Rujula, E. Fernandez and J.J. Gomez-Cadenas, *Neutrino fluxes at future hadron colliders*, *Nucl. Phys.* **B405** (1993) 80.
- [14] F. Vannucci, *Neutrino physics at LHC / SSC*, in *5th International Symposium on Neutrino Telescopes Venice, Italy, March 2-4, 1993*, pp. 57–68, 1993, <http://lss.fnal.gov/archive/other/lpnhe-93-03.pdf>.
- [15] W. Bai, M. Diwan, M.V. Garzelli, Y.S. Jeong and M.H. Reno, *Far-forward neutrinos at the Large Hadron Collider*, *JHEP* **06** (2020) 032 [[2002.03012](#)].
- [16] W. Bai, M. Diwan, M.V. Garzelli, Y.S. Jeong, F.K. Kumar and M.H. Reno, *Parton distribution function uncertainties in theoretical predictions for far-forward tau neutrinos at the Large Hadron Collider*, *JHEP* **06** (2022) 148 [[2112.11605](#)].
- [17] W. Bai, M.V. Diwan, M.V. Garzelli, Y.S. Jeong, K. Kumar and M.H. Reno, *Prompt electron and tau neutrinos and antineutrinos in the forward region at the LHC*, *JHEAp* **34** (2022) 212 [[2203.07212](#)].
- [18] F. Kling and L.J. Nevay, *Forward neutrino fluxes at the LHC*, *Phys. Rev. D* **104** (2021) 113008 [[2105.08270](#)].
- [19] FASER collaboration, *Detecting and Studying High-Energy Collider Neutrinos with FASER at the LHC*, *Eur. Phys. J. C* **80** (2020) 61 [[1908.02310](#)].
- [20] FASER collaboration, *The FASER Detector*, [2207.11427](#).
- [21] SHiP collaboration, *SND@LHC*, [2002.08722](#).
- [22] SND@LHC collaboration, *SND@LHC: The Scattering and Neutrino Detector at the LHC*, [2210.02784](#).
- [23] FASER collaboration, *First neutrino interaction candidates at the LHC*, *Phys. Rev. D* **104** (2021) L091101 [[2105.06197](#)].
- [24] L.A. Anchordoqui et al., *The Forward Physics Facility: Sites, experiments, and physics potential*, *Phys. Rept.* **968** (2022) 1 [[2109.10905](#)].

- [25] J.L. Feng et al., *The Forward Physics Facility at the High-Luminosity LHC*, [2203.05090](#).
- [26] M. Ackermann et al., *High-energy and ultra-high-energy neutrinos: A Snowmass white paper*, *JHEAp* **36** (2022) 55 [[2203.08096](#)].
- [27] ICECUBE collaboration, *First observation of PeV-energy neutrinos with IceCube*, *Phys. Rev. Lett.* **111** (2013) 021103 [[1304.5356](#)].
- [28] ICECUBE collaboration, *Characteristics of the diffuse astrophysical electron and tau neutrino flux with six years of IceCube high energy cascade data*, *Phys. Rev. Lett.* **125** (2020) 121104 [[2001.09520](#)].
- [29] ICECUBE collaboration, *The IceCube high-energy starting event sample: Description and flux characterization with 7.5 years of data*, *Phys. Rev. D* **104** (2021) 022002 [[2011.03545](#)].
- [30] P. Lipari, *Lepton spectra in the earth's atmosphere*, *Astropart. Phys.* **1** (1993) 195.
- [31] T.K. Gaisser, R. Engel and E. Resconi, *Cosmic Rays and Particle Physics: 2nd Edition*, Cambridge University Press (6, 2016).
- [32] R. Enberg, M.H. Reno and I. Sarcevic, *Prompt neutrino fluxes from atmospheric charm*, *Phys. Rev. D* **78** (2008) 043005 [[0806.0418](#)].
- [33] PROSA collaboration, *Prompt neutrino fluxes in the atmosphere with PROSA parton distribution functions*, *JHEP* **05** (2017) 004 [[1611.03815](#)].
- [34] M. Benzke, M.V. Garzelli, B. Kniehl, G. Kramer, S. Moch and G. Sigl, *Prompt neutrinos from atmospheric charm in the general-mass variable-flavor-number scheme*, *JHEP* **12** (2017) 021 [[1705.10386](#)].
- [35] PROSA collaboration, *Improved constraints on parton distributions using LHCb, ALICE and HERA heavy-flavour measurements and implications for the predictions for prompt atmospheric-neutrino fluxes*, *JHEP* **04** (2020) 118 [[1911.13164](#)].
- [36] S. Ostapchenko, M.V. Garzelli and G. Sigl, *On the prompt contribution to the atmospheric neutrino flux*, [2208.12185](#).
- [37] R. Gauld, J. Rojo, L. Rottoli, S. Sarkar and J. Talbert, *The prompt atmospheric neutrino flux in the light of LHCb*, *JHEP* **02** (2016) 130 [[1511.06346](#)].
- [38] A. Bhattacharya, R. Enberg, M.H. Reno, I. Sarcevic and A. Stasto, *Perturbative charm production and the prompt atmospheric neutrino flux in light of RHIC and LHC*, *JHEP* **06** (2015) 110 [[1502.01076](#)].
- [39] A. Bhattacharya, R. Enberg, Y.S. Jeong, C.S. Kim, M.H. Reno, I. Sarcevic et al., *Prompt atmospheric neutrino fluxes: perturbative QCD models and nuclear effects*, *JHEP* **11** (2016) 167 [[1607.00193](#)].
- [40] ICECUBE collaboration, *Observation and Characterization of a Cosmic Muon Neutrino Flux from the Northern Hemisphere using six years of IceCube data*, *Astrophys. J.* **833** (2016) 3 [[1607.08006](#)].
- [41] Y.S. Jeong, W. Bai, M. Diwan, M.V. Garzelli, F.K. Kumar and M.H. Reno, *Neutrinos from charm: forward production at the LHC and in the atmosphere*, *PoS ICRC2021* (2021) 1218 [[2107.01178](#)].

- [42] P. Nason, S. Dawson and R.K. Ellis, *The One Particle Inclusive Differential Cross-Section for Heavy Quark Production in Hadronic Collisions*, *Nucl. Phys.* **B327** (1989) 49.
- [43] M.L. Mangano, P. Nason and G. Ridolfi, *Heavy quark correlations in hadron collisions at next-to-leading order*, *Nucl. Phys.* **B373** (1992) 295.
- [44] LHCb collaboration, *Prompt charm production in pp collisions at $\sqrt{s}=7$ TeV*, *Nucl. Phys. B* **871** (2013) 1 [[1302.2864](#)].
- [45] LHCb collaboration, *Measurements of prompt charm production cross-sections in pp collisions at $\sqrt{s} = 13$ TeV*, *JHEP* **03** (2016) 159 [[1510.01707](#)].
- [46] LHCb collaboration, *Measurement of D_s^\pm production asymmetry in pp collisions at $\sqrt{s} = 7$ and 8 TeV*, *JHEP* **08** (2018) 008 [[1805.09869](#)].
- [47] W. Bai and M.H. Reno, *Prompt neutrinos and intrinsic charm at SHiP*, *JHEP* **02** (2019) 077 [[1807.02746](#)].
- [48] FCC collaboration, *FCC-hh: The Hadron Collider: Future Circular Collider Conceptual Design Report Volume 3*, *Eur. Phys. J. ST* **228** (2019) 755.
- [49] M. Benedikt and F. Zimmermann, *Future Circular Collider: Integrated Programme and Feasibility Study*, *Front. in Phys.* **10** (2022) 888078.
- [50] T.K. Gaisser, D. Soldin, A. Crossman and A. Fedynitch, *Precision of analytical approximations in calculations of Atmospheric Leptons*, *PoS ICRC2019* (2020) 893 [[1910.08676](#)].
- [51] P. Gondolo, G. Ingelman and M. Thunman, *Charm production and high-energy atmospheric muon and neutrino fluxes*, *Astropart. Phys.* **5** (1996) 309 [[hep-ph/9505417](#)].
- [52] A. Coleman et al., *Ultra-High-Energy Cosmic Rays: The Intersection of the Cosmic and Energy Frontiers*, [2205.05845](#).
- [53] T.K. Gaisser, *Spectrum of cosmic-ray nucleons, kaon production, and the atmospheric muon charge ratio*, *Astropart. Phys.* **35** (2012) 801 [[1111.6675](#)].
- [54] K.-H. Kampert and M. Unger, *Measurements of the Cosmic Ray Composition with Air Shower Experiments*, *Astropart. Phys.* **35** (2012) 660 [[1201.0018](#)].
- [55] TELESCOPE ARRAY collaboration, *The Cosmic-Ray Composition between 2 PeV and 2 EeV Observed with the TALE Detector in Monocular Mode*, *Astrophys. J.* **909** (2021) 178 [[2012.10372](#)].
- [56] D.P. Bowman, R. Scrandis and E.-S. Seo, *Investigating cosmic ray elemental spectra and the atmospheric muon neutrino flux*, *Adv. Space Res.* **70** (2022) 2703.
- [57] S. Dulat, T.-J. Hou, J. Gao, M. Guzzi, J. Huston, P. Nadolsky et al., *New parton distribution functions from a global analysis of quantum chromodynamics*, *Phys. Rev. D* **93** (2016) 033006 [[1506.07443](#)].
- [58] S. Alekhin, J. Blümlein and S. Moch, *NLO PDFs from the ABMP16 fit*, *Eur. Phys. J. C* **78** (2018) 477 [[1803.07537](#)].
- [59] NNPDF collaboration, *Parton distributions from high-precision collider data*, *Eur. Phys. J. C* **77** (2017) 663 [[1706.00428](#)].

- [60] NNPDF collaboration, *The path to proton structure at 1% accuracy*, *Eur. Phys. J. C* **82** (2022) 428 [[2109.02653](#)].
- [61] B. Andersson, G. Gustafson and C. Peterson, *A Semiclassical Model for Quark Jet Fragmentation*, *Z. Phys. C* **1** (1979) 105.
- [62] LHCb collaboration, *Measurement of the $D_s^+ - D_s^-$ production asymmetry in 7 TeV pp collisions*, *Phys. Lett. B* **713** (2012) 186 [[1205.0897](#)].
- [63] LHCb collaboration, *Measurement of D_s^\pm production asymmetry in pp collisions at $\sqrt{s} = 7$ and 8 TeV*, *JHEP* **08** (2018) 008 [[1805.09869](#)].
- [64] V.P. Goncalves, R. Maciula, R. Pasechnik and A. Szczurek, *Mapping the dominant regions of the phase space associated with $c\bar{c}$ production relevant for the prompt atmospheric neutrino flux*, *Phys. Rev. D* **96** (2017) 094026 [[1708.03775](#)].
- [65] ICECUBE-GEN2 collaboration, *IceCube-Gen2: the window to the extreme Universe*, *J. Phys. G* **48** (2021) 060501 [[2008.04323](#)].
- [66] SND@LHC collaboration, *Status of SND@LHC (Scattering and Neutrino Detector at the LHC)*, *PoS NuFact2021* (2022) 158.
- [67] M. Honda, T. Kajita, K. Kasahara, S. Midorikawa and T. Sanuki, *Calculation of atmospheric neutrino flux using the interaction model calibrated with atmospheric muon data*, *Phys. Rev. D* **75** (2007) 043006 [[astro-ph/0611418](#)].
- [68] C. Hadjidakis et al., *High-luminosity fixed-target experiments at the LHC*, *PoS HardProbes2018* (2019) 041 [[1902.10534](#)].
- [69] J. Albrecht et al., *The Muon Puzzle in cosmic-ray induced air showers and its connection to the Large Hadron Collider*, *Astrophys. Space Sci.* **367** (2022) 27 [[2105.06148](#)].
- [70] ICECUBE collaboration, *Characterization of the Atmospheric Muon Flux in IceCube*, *Astropart. Phys.* **78** (2016) 1 [[1506.07981](#)].
- [71] ICECUBE collaboration, *Development of a Machine Learning Based Analysis Chain for the Measurement of Atmospheric Muon Spectra with IceCube*, in *25th European Cosmic Ray Symposium*, 1, 2017 [[1701.04067](#)].
- [72] ICECUBE collaboration, *Atmospheric Muons Measured with IceCube*, *EPJ Web Conf.* **208** (2019) 08007 [[1811.03651](#)].